SFN 341 #1 - #6 西合 一矢 (国立天文台)

2021/6/11発表

1. The stellar content of H72.97-69.39, a potential super star cluster in the making
   M. Andersen, H. Zinnecker, A. S. Hirschauer, O. Nayak, M. Meixner
   https://arxiv.org/pdf/2102.06544.pdf

2. ALMA Observations toward the S-shaped Outflow and the Envelope around NGC1333 IRAS 4A2
   Chen-Yu Chuang, Yusuke Aso, Naomi Hirano, Shingo Hirano, Masahiro N. Machida
   https://arxiv.org/pdf/2105.04224.pdf

3. Variation of the Core Lifetime and Fragmentation Scale in Molecular Clouds as an Indication of Ambipolar Diffusion
   Indrani Das, Shantanu Basu, Philippe Andre
   https://arxiv.org/pdf/2104.10179.pdf

4. 1I/'Oumuamua as an N2 ice fragment of an exo-pluto surface. II. Generation of N2 ice fragments and the origin of 'Oumuamua
   Steven J. Desch, Alan P. Jackson
   https://arxiv.org/pdf/2103.08812.pdf

5. Estimate on dust scale height from ALMA dust continuum image of the HD 163296 protoplanetary disk
   Kiyoaki Doi, Akimasa Kataoka
   https://arxiv.org/pdf/2102.06209.pdf

6. Two-component Magnetic Field along the Line of Sight to the Perseus Molecular Cloud: Contribution of the Foreground Taurus Molecular Cloud
   Y. Doi, T. Hasegawa, P. Bastien, M. Tahani, D. Arzoumanian, S. Coudé, M. Matsumura, S. Sadavoy, C. L. H. Hull, Y. Shimajiri, R. S. Furuya, D. Johnstone, R. Plume, S. Inutsuka, J. Kwon, M. Tamura
   https://arxiv.org/pdf/2104.11932.pdf

The stellar content of H72.97-69.39, a potential super star cluster in the making

M. Andersen, H. Zinnecker, A. S. Hirschauer, O. Nayak, M. Meixner

https://arxiv.org/pdf/2102.06544.pdf

Abstract

Young massive clusters and super star clusters (SSCs) represent an extreme mode of star formation. Far-infrared imaging of the Magellanic Clouds has identified one potential embedded SSC, HSO BMHERICC J72.971176-69.391112 (H72.97-69.39 in short), in the southwest outskirts of the Large Magellanic Cloud. We present Gemini Flamingos 2 and GSAOI near-infrared imaging of a $3' \times 3'$ region around H72.97-69.39 in order to characterize the stellar content of the cluster. The stellar content is probed down to 1.5 $M_\odot$. We find substantial dust extinction across the cluster region, extending up to A_K of 3. Deeply embedded stars are associated with ALMA-detected molecular gas suggesting that star formation is ongoing. The high spatial resolution of the GSAOI data allows identification of the central massive object associated with the ^{13}CO ALMA observations and detection of fainter low-mass stars around the H30α ALMA source. The morphology of the molecular gas and the nebulosity from adjacent star formation suggest they have interacted covering a region of several parsecs. The total stellar content in the cluster is estimated from the intermediate- and high-mass stellar content to be at least 10,000 $M_\odot$, less than R136 with up to 100,000 $M_\odot$ within 4.7 pc radius, but places it in the regime of an SSC. Based on the extinction determination of individual stars we estimate a molecular gas mass in the vicinity of H72.97-69.39 of 6600 $M_\odot$, suggesting more star formation can be expected.

Large Magellanic Cloudにある星団 H72.97−69.39をGemini Flamingos 2とGASOIを用いて高分解能観測を行った。
星分布や年齢と減光量から、この星団はr< ～1.7pcに7200M$_\odot$の星成分を持ち、同時に同じ程度のガス成分を持つ非常に若い。H72.97−69.39はSuper Star Cluster形成初期の天体である可能性があり貴重なサンプルである。

GeminiのFlamingos 2によるJHK合成イメージ

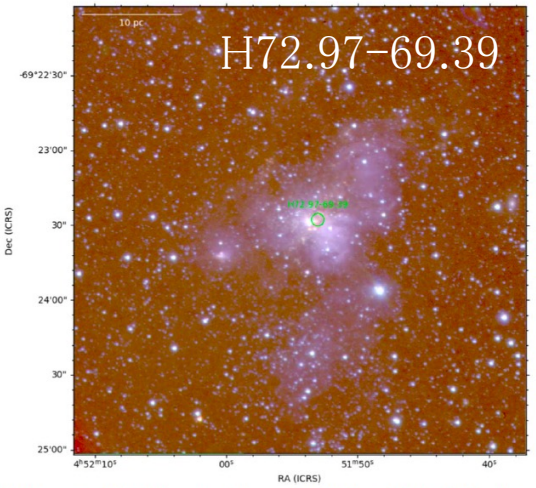

Figure 1. Flamingos 2 *JHKs* color composite of N79 and its surroundings. Blue represents the *J* band, green *H*, and red K_s. A logarithmic scale for all three channels has been used. The field of view shown is $3' \times 3'$, corresponding to 43 pc × 43 pc. The whole nebulous region shown has previously been identified as IC2111. The location of H72.97-69.39 is marked with the green circle, the size (5″) of the Herschel beam.

観測結果

GeminiのGASOIのHKsのAOイメージ(fig.4)

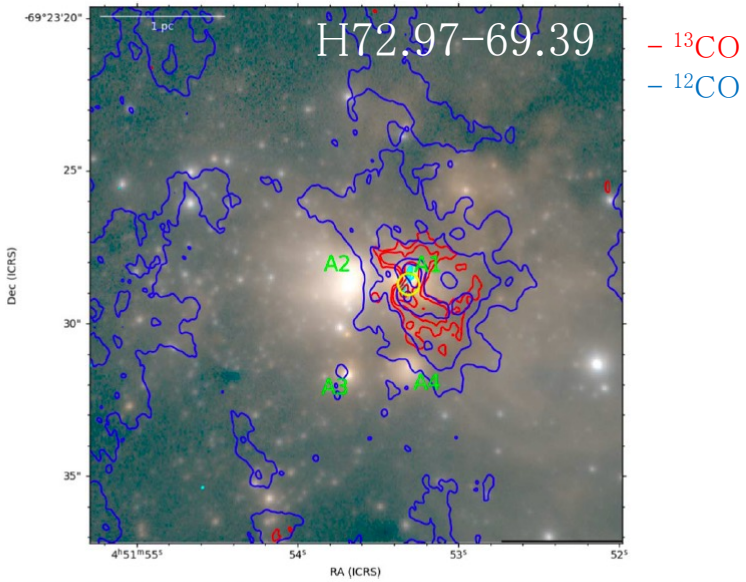

Figure 4. The central region around H72.97-69.39. Several filamentary dark lanes are present obscuring parts of the stellar content even at near-infrared wavelengths. Overplotted as contours are the SO integrated emission (cyan), the ^{13}CO integrated emission in red, and the ^{12}CO integrated emission in blue (Nayak et al. 2019). The location of the H30α source is further marked as a yellow circle. The spatial resolution of the ALMA 1.3 mm observations is $0\farcs3 \times 0\farcs2$. Several bright sources associated with nebulosity have been marked as A1 (the ATCA source), A2 (the approximate cluster center), A3, and A4.

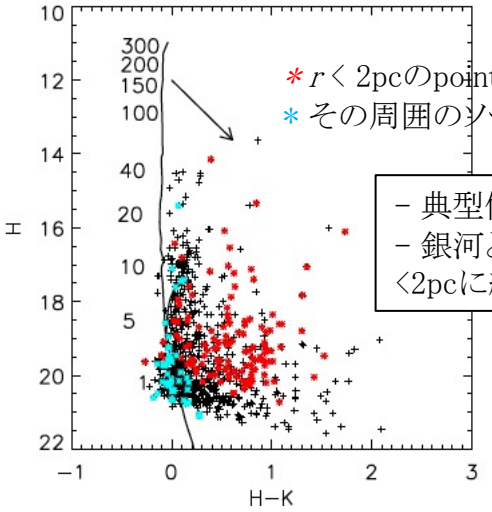

Fig 5. Point sourceと1Myrの isochrone

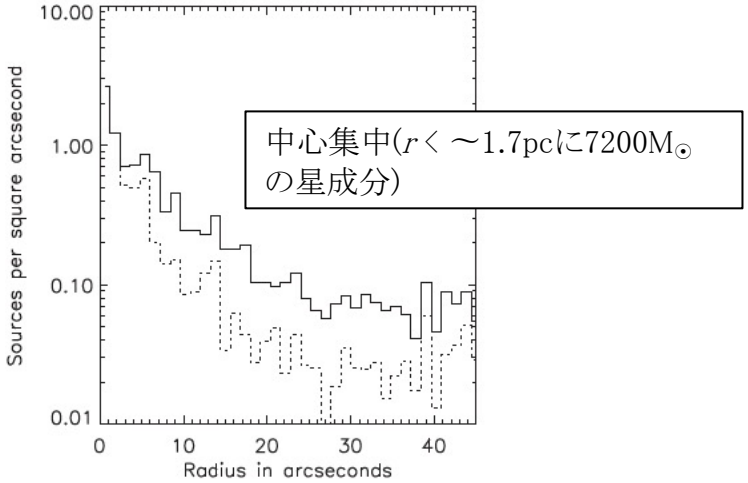

Fig 6. 星の半径方向の分布。点線は明るい星(H<19.5)。

結論

– H72.97-69.39 は、r＜ ～1.7pcに7200M⊙の中心集中した若い星成分を持つ(これはR136の5分の1)。
– 減光(Ak)から見積もられるガス成分はr＜2で76580M⊙である(R136はガスが少ない) 。

=> これらから、H72.97-69.39 はR136より遥かに若く*Super Star Cluster(SSC)になる可能性を秘めた*星団形成初期の天体であると言える。

ALMA Observations toward the S-shaped Outflow and the Envelope around NGC1333 IRAS 4A2

Chen-Yu Chuang, Yusuke Aso, Naomi Hirano, Shingo Hirano, Masahiro N. Machida

https://arxiv.org/pdf/2105.04224.pdf

Abstract

We have analyzed the ALMA archival data of the SO ($J_N = 6_5 - 5_4$ and $J_N = 7_6 - 6_5$), CO ($J = 2-1$), and CCH ($N = 3-2, J = 7/2-5/2, F = 4-3$) lines from the class 0 protobinary system, NGC1333 IRAS 4A. The images of SO ($J_N = 6_5 - 5_4$) and CO ($J = 2-1$) successfully separate two northern outflow lobes connected to each protostar, IRAS 4A1 and IRAS 4A2. The outflow from IRAS 4A2 shows an S-shaped morphology, consisting of a flattened envelope around IRAS 4A2 with two outflow lobes connected to both edges of the envelope. The flattened envelope surrounding IRAS 4A2 has an opposite velocity gradient to that of the circumbinary envelope. The observed features are reproduced by the magnetohydrodynamic simulation of the collapsing core whose magnetic field direction is misaligned to the rotational axis. Our simulation shows that the intensity of the outflow lobes is enhanced on one side, resulting in the formation of S-shaped morphology. The S-shaped outflow can also be explained by the precessing outflow launched from an unresolved binary with a separation larger than 12 au (0.04arcsec). Additionally, we discovered a previously unknown extremely high velocity component at ~45-90 km/s near IRAS 4A2 with CO. CCH ($J_{N,F} = 7/2_{3,4} - 5/2_{2,3}$) emission shows two pairs of blobs attaching to the bottom of shell like feature, and the morphology is significantly different from those of SO and CO lines. Toward IRAS 4A2, the S-shaped outflow shown in SO is overlapped with the edges of CCH shells, while CCH shells have the velocity gradients opposite to the flattened structure around IRAS 4A2.

ALMA archiveデータを用いて原始星連星NGC1333 4A2の特殊なoutflow 構造 (S-shaped構造)を明確に示し、各種物理量を導出した。さらにMHD simulationとの比較により、このS-shaped構造は**原始星円盤とエンベロープの回転軸がmisalignedしたモデルで説明可能**であることを示した。

観測データ

ALMA Archive data (2013.1.01102 in 262GHz, 2017.1.00053, 2013.1.00031 in 230GHz).
Continuum(0.26”x0.16”) + Lines SO(6_5–5_4), SO(7_6–6_5), 12CO(2–1), CCH(3–2)
NGC1333 IRAS 4A1 4A2: *d* ～ 300pcにあるClass 0 連星系 (separation = 1.8”)

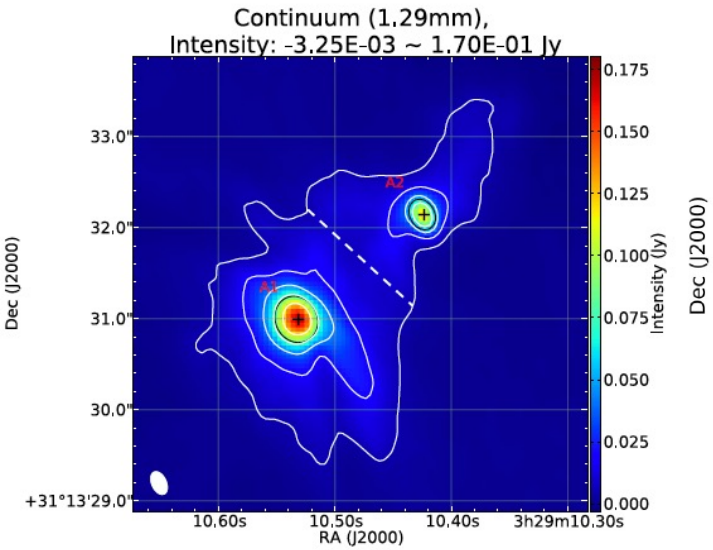

Fig.1 ダスト連続波image

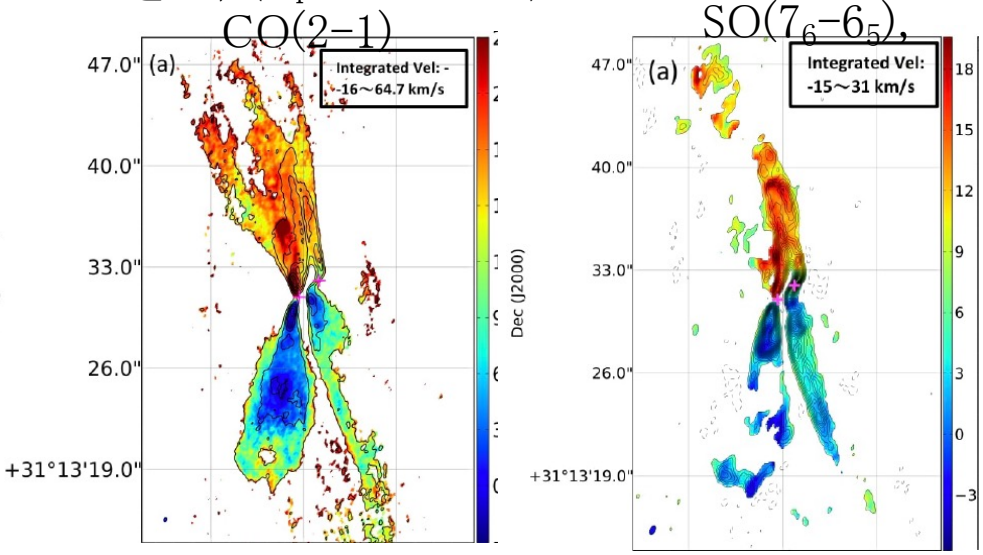

Fig.2a CO(2-1) とFig.4a(SO) のmoment 1 map(カラー)、コントアは*momen0*. OutflowがS–Shapeとなっている(この構造は知られていたが高い分解能でより詳細に見えた)

考察とMHD計算

S–Shapeの原因考察

- Rotation of the Outflow => X 回転方向が合わない
- Precsession by Close Binary => X closed binaryででないと再現できない。
- Magnetic Field Misalignment Model => ○ (右のfigure 11)

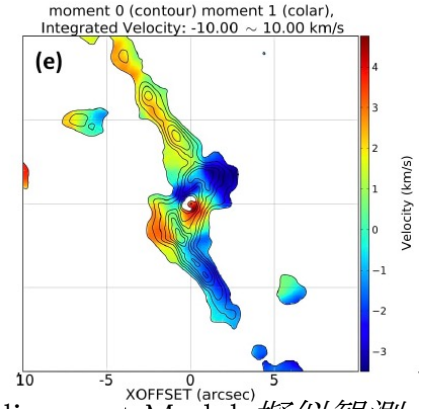

Fig.11 Magnetic Field Misalignment Model *擬似観測*

Variation of the Core Lifetime and Fragmentation Scale in Molecular Clouds as an Indication of Ambipolar Diffusion

Indrani Das, Shantanu Basu, Philippe Andre

https://arxiv.org/pdf/2102.06544.pdf

星形成における分子雲コアのタイムスケールと分裂片スケールに対して、両極拡散(ambipolar-diffusion)を含む線形解析モデルを構築し、Herschelなどのいくつかのサーベイ観測と比較した。
結果として、磁場なしの乱流モデルでは、観測が示す密度に対して分子雲コアのタイムスケールや分裂構造の系統的な変化を説明できないことがわかった。分子雲コアはややsupercritical(やや重力不安定)、かつ磁場強度 ∝ (密度)^0.427 であるとすると観測を説明できる。これは、ambipolar-diffusionがコアの重力崩壊進化に影響していることを示唆している。

分子雲コアの重力崩壊進化

統計的に分子雲コアは寿命～1Myr (～4 free-fall timescale)で星を形成すると思われている。
その進化初期に*両極拡散(ambipolar-diffusion)*、*乱流*、*converging flow*など重要な働きをすることがMHD simulationにより示唆されている。しかし、観測的にはそれらの影響の差を明確化できてない。

Normalized mass-to-flux ratio $\mu_0 \equiv 2\pi G^{1/2} \frac{\sigma_{n,0}}{B_{\rm ref}}$, (3)

$\mu_0 < 1$ subcritical (磁場優勢), $\mu_0 \sim 1$ trans-subcritical, $\mu_0 > 1$ supercritical (重力優勢)

モデル

分子雲コアの重力崩壊モデルとして、無限に広い平面での等温ガスの自己重力シート状磁気雲における両極拡散駆動(弱電離)の線形解析を採用する。ただし、

- neutral-ion collision rate (between H_2 and HCO^+) = 1.69×10^{-9} cm^3 s^{-1} (MacDaniel &Mason 1973)
- 電離率 $\chi_i = 10^{-7}\left(\frac{n_{n,0}}{10^4\ {\rm cm}^{-3}}\right)^{-1/2}$. (2)
- 磁場強度 $\frac{B_{\rm ref}}{10\,\mu{\rm G}} = A\left(\frac{n_n}{10^4\ {\rm cm}^{-3}}\right)^{\kappa}$, (7)

こういう関数系を仮定

分散方程式

$$(\omega + i\,\theta)\left[\omega^2 - C_{\mathrm{eff},0}^2\,k^2 + 2\pi G\sigma_{n,0}k\right] = \omega\left[2\pi G\sigma_{n,0}k\mu_0^{-2} + k^2\,V_{A,0}^2\right], \quad (4)$$

where

$$\theta = \tau_{ni,0}\left(2\pi G\sigma_{n,0}\mu_0^{-2}k + k^2V_{A,0}^2\right) = \eta_{\mathrm{AD},0}(k\,Z_0^{-1} + k^2), \quad (5)$$

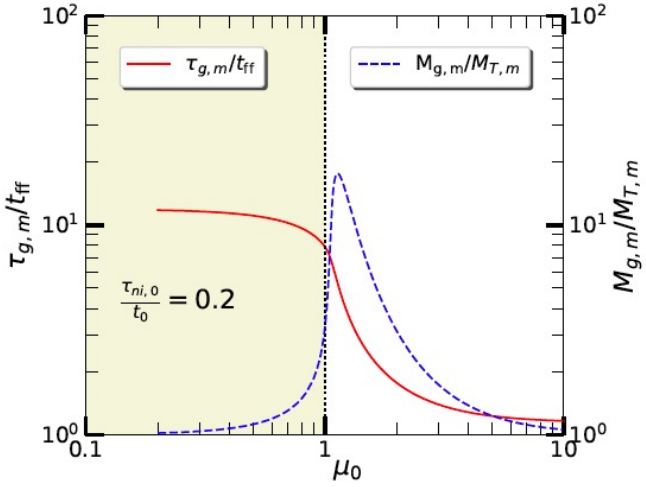

Fig 1.Growth timescale $\tau_{g,m}$と分裂質量

観測との比較 I

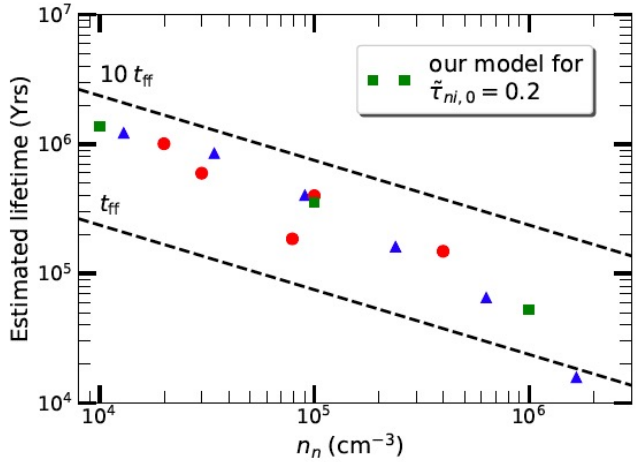

Fig. 2: Estimated lifetime as a function of number density (n_n). The green filled squares are obtained from our model for a normalized neutral-ion collision time $\tilde{\tau}_{ni,0} = 0.2$. The blue filled triangles show the corresponding data points for the population of 446 candidate prestellar cores identified with *Herschel* in the Aquila cloud (Könyves et al. 2015). Earlier data from Ward-Thompson et al. (2007) is shown by the red circles for better comparison. The black dashed line shows the dynamical time (Z_0/c_s), i.e., the free-fall time, of our model.

- ▲ AquilaでのHerschelからのタイムスケール見積もり
- ● IRAS all skyサーベイからの見積もり
- ■ 今回のモデル(磁場強度はベストfit→) $\frac{B_{\mathrm{ref}}}{10\,\mu\mathrm{G}} = A\left(\frac{n_n}{10^4\ \mathrm{cm}^{-3}}\right)^{\kappa}$,
  where $\kappa = 0.427$ and $A = 1.766$,
  数値はTable B.1参照

Table B.1: Fitting Data for Calculating the Lifetime of Prestellar Cores

n_n ($\times 10^5$ cm^{-3})	μ	σ_n ($\times 10^{-2}$ g cm^{-2})	B_{ref} (μG)	Estimated lifetime of prestellar cores (Myr)
0.1	1.080	1.094	16.45	1.371 ($\sim 5.777\ t_{\mathrm{ff}}$)
1	1.125	3.461	49.94	0.355 ($\sim 4.728\ t_{\mathrm{ff}}$)
10	1.486	10.944	119.57	0.053 ($\sim 2.220\ t_{\mathrm{ff}}$)

観測との比較 II

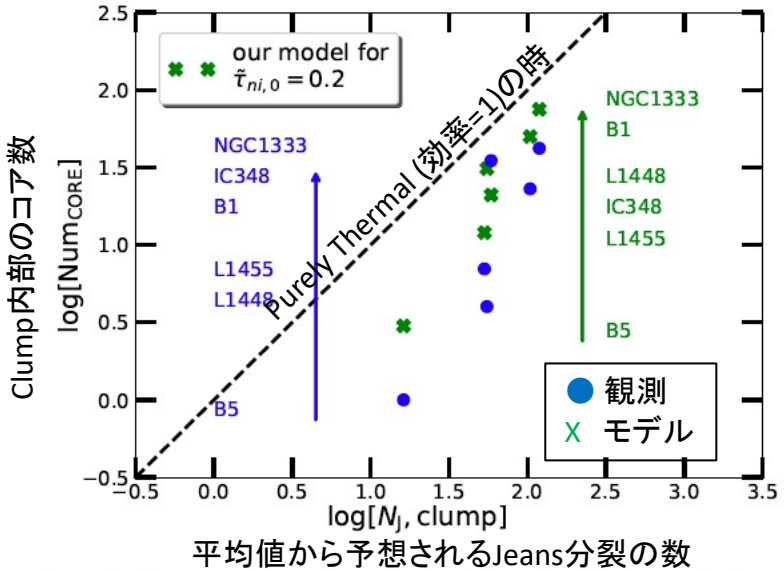

Fig. 3: The number of enclosed cores (log[Num$_{CORE}$]) as a function of Jeans number (log[$N_{J,CLUMP}$]) of clumps. The blue filled circles represent the observed number of enclosed cores as found by Pokhrel et al. (2018). The green filled crosses are obtained from our model for a normalized neutral-ion collision time $\tilde{\tau}_{ni,0} = 0.2$. The black dashed line corresponds to an efficiency of unity.

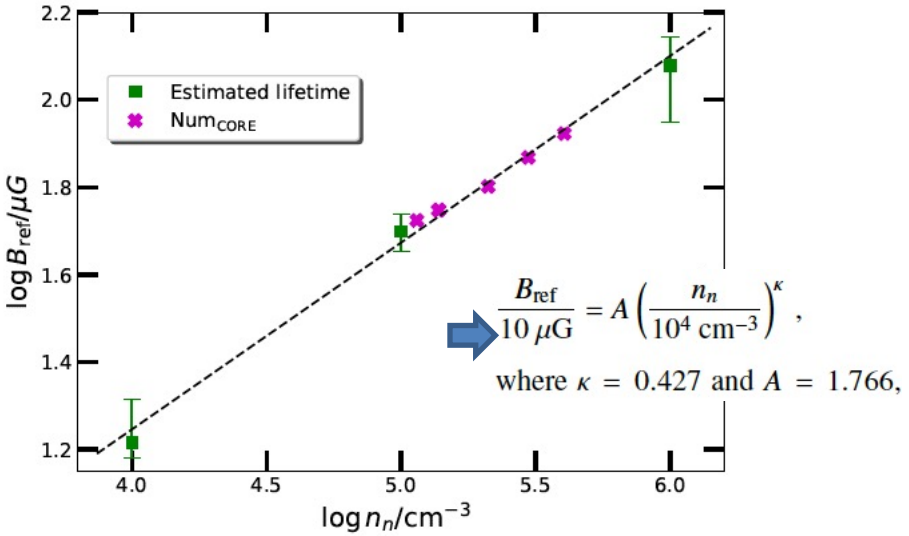

Fig. 4: Magnetic field log(B_{ref}/μG) versus number density log(n_n/cm^{-3}). The filled squares and crosses represent the number density region corresponding to the fitting of the lifetime of prestellar cores and Num$_{CORE}$ as shown in Figure 2 and Figure 3 (see Table B.1 & Table B.2). The dashed line is the least-squares fit. The vertical error bars correspond to magnetic field variations that yield a total factor of 2 (greater or lesser by a factor $\sqrt{2}$) values of the growth time (lifetime).

参考

Table B.2: Fitting Data for Calculating the Number of Enclosed Cores (Num$_{CORE}$)

Clump name	Clump Mass ($M_\odot$)	Area (pc^2)	$\sigma_n \times 10^{-2}$ (g cm^{-2})	$n_n \times 10^5$ (cm^{-3})	μ	B_{ref} (μG)	$M_{g,m}$ ($M_\odot$)	N_J^{th}	$N_J^{th,nth}$	Num$_{CORE}$	ϵ^{th}	$\epsilon^{th,nth}$
B5	62	0.32	4.064	1.383	1.178	56.01	20.165	16.2	1.5	3	0.185	2.000
L1455	251	1.3	4.050	1.373	1.176	55.90	20.339	53.1	4.3	12	0.226	2.791
IC348	511	2.9	3.697	1.144	1.132	53.00	23.858	58.6	6.4	21	0.358	3.281
L1448	159	0.48	6.948	4.042	1.470	76.73	5.108	55.1	4.6	31	0.562	6.739
B1	598	2.5	5.018	2.107	1.286	63.34	11.738	103.9	9.5	50	0.481	5.263
NGC1333	568	2.0	5.958	2.971	1.379	70.13	7.508	119	10.5	75	0.630	7.142

Notes. [a] Clump name, Clump Mass, Area, N_J^{th}, $N_J^{th,nth}$ are taken from Table 2 of Pokhrel et al. (2018).
[b] In the above table, n_n, σ_n, μ, B_{ref}, $M_{g,m}$, Num$_{CORE}$, ϵ^{th}, $\epsilon^{th,nth}$ are evaluated based on our model. Here, σ_n is the clump mass per unit area, n_n is obtained using Equation A.5, μ is a free parameter of our model, B_{ref} is calculated using Equation 3, and $M_{g,m}$ is obtained based on Figure 1, Num$_{CORE}$ = Clump Mass/$M_{g,m}$, ϵ^{th} = Num$_{CORE}$/N_J^{th}, $\epsilon^{th,nth}$ = Num$_{CORE}$/$N_J^{th,nth}$.
[c] Table B.2 is arranged in the ascending order of Num$_{CORE}$.

1I/'Oumuamua as an N2 ice fragment of an exo-pluto surface. II. Generation of N2 ice fragments and the origin of 'Oumuamua

Steven J. Desch, Alan P. Jackson ★

The origin of the interstellar object 1I/'Oumuamua, has defied explanation. In a companion paper (Jackson & Desch, 2021), we show that a body of N2 ice with axes 45 m x 44 m x 7.5 m at the time of observation would be consistent with its albedo, non-gravitational acceleration, and lack of observed CO or CO2 or dust. Here we demonstrate that impacts on the surfaces of Pluto-like Kuiper belt objects (KBOs) would have generated and ejected 10^14 collisional fragments–roughly half of them H2O ice fragments and half of them N2 ice fragments–due to the dynamical instability that depleted the primordial Kuiper belt. We show consistency between these numbers and the frequency with which we would observe interstellar objects like 1I/'Oumuamua, and more comet-like objects like 2I/Borisov, if other stellar systems eject such objects with efficiency like that of the Sun; we infer that differentiated KBOs and dynamical instabilities that eject impact-generated fragments may be near-universal among extrasolar systems. Galactic cosmic rays would erode such fragments over 4.5 Gyr, so that fragments are a small fraction (0.1%) of long-period Oort comets, but C/2016 R2 may be an example. We estimate 'Oumuamua was ejected about 0.4-0.5 Gyr ago, from a young (10^8 yr) stellar system, which we speculate was in the Perseus arm. Objects like 'Oumuamua may directly probe the surface compositions of a hitherto-unobserved type of exoplanet: "exo-plutos". 'Oumuamua may be the first sample of an exoplanet brought to us.

太陽系外から飛来したOumunauaのアルベドはN_2 iceで説明でき、CO/CO2/dustなどは見られなかった。
N_2 iceの塊は冥王星やカイパーベルト天体のような天体の衝突により生成が可能であり、そのような衝突は若い惑星系天体でより頻発する。
また、一般にN_2 iceは宇宙線により1Gyrあたり数10m侵食されることから、典型的には0.4−0.5Gyr程度の年齢と推定できる。
これらからOumunauaは系外の若い惑星系において冥王星やカイパーベルト天体のような外縁天体の衝突により生成され放出されたと考えられる。

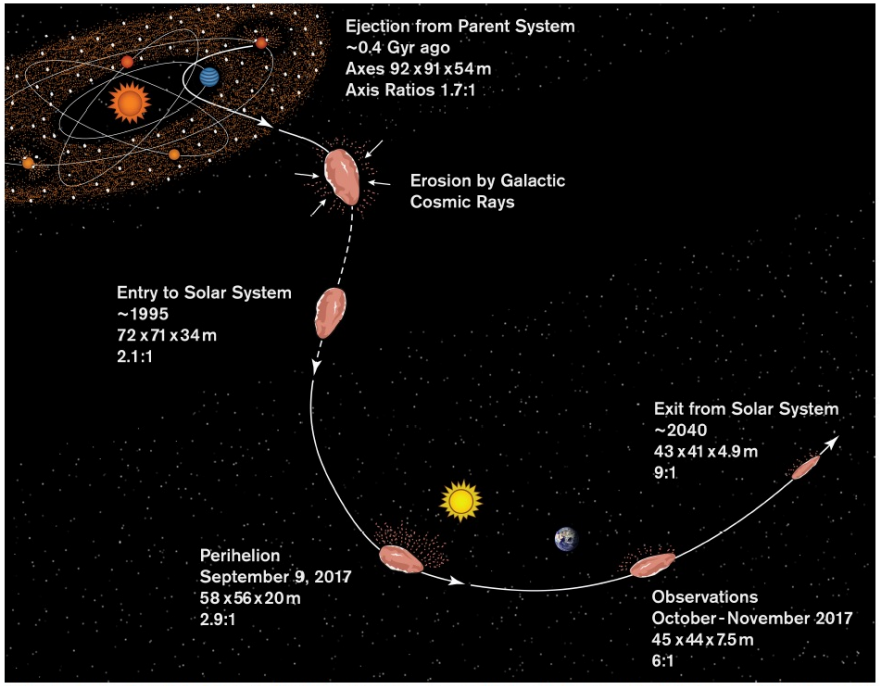

Figure 1. A plausible history for 'Oumuamua as a collisional fragment of N_2 ice, as hypothesized in this paper and the companion paper by Jackson and Desch (2021). *Credit*: Sue Selkirk.

Estimate on dust scale height from ALMA dust continuum image of the HD 163296 protoplanetary disk

Kiyoaki Doi, Akimasa Kataoka

https://arxiv.org/pdf/2102.06209.pdf

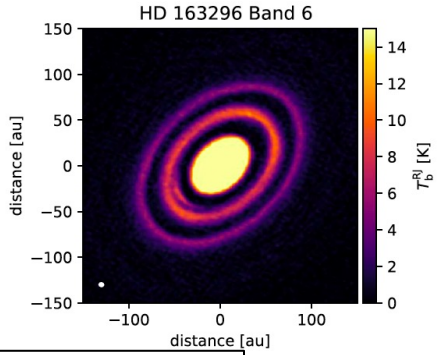

HD 163296の原始惑星系円盤に見られるリング構造(r=68 au and 100 au)の方位角の強度変化からダストのスケールハイトを調べた。
結果は、内リング(r=68)で $h_d/h_g > 0.84$、外リング(r=100au) で $h_d/h_g < 0.11$と内リングのダストがフレアし外リングのダストが沈殿しているというものであった。また、乱流パラメータ α とガス対ダスト カップリング パラメータ St の比率についても内リングで $\alpha/St > 2.4$、外リングで $\alpha/St < 1.1\times10^{-2}$と制約できた。これは外リングより内リングの方が乱流が強いかダストが少ないことを示唆する。

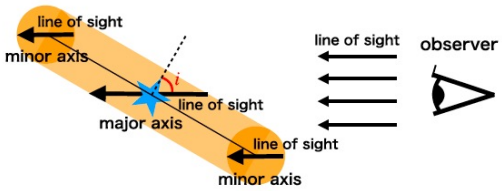

Fig 1.

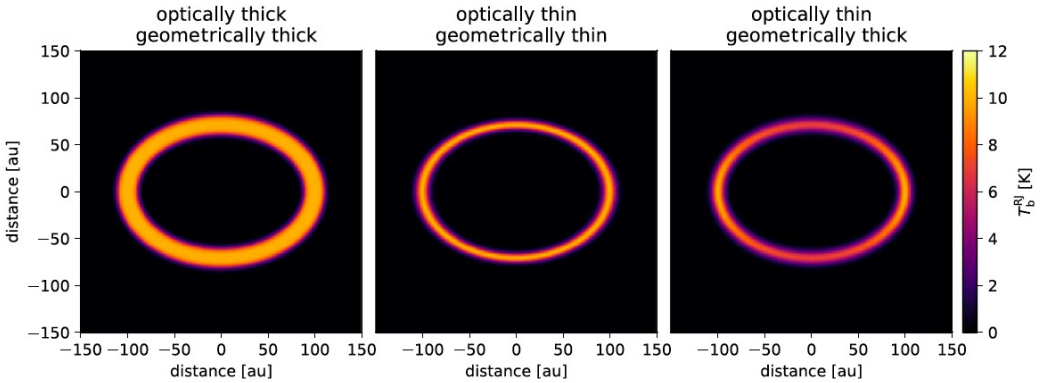

Fig 2. 2Dガウシアンリングモデルでの方位角変動のデモンストレーション

HD163296 観測情報

d = 101.5 pc, M_{star} = 2.02$M_\odot$, i = 46.7deg

Table 1
Parameters of the Dust Rings of HD 163296

Ring (1)	r_0 (au) (2)	Σ_{dust} (g cm^{-2}) (3)	w_{dust} (au) (4)	h_{gas} (au) (5)
inner ring	67.9	1.26	4.0	3.8
outer ring	100.5	0.58	3.9	6.7

$$\Sigma_{disk} = 20.66\ \mathrm{g\ cm^{-2}},\quad r_{disk} = 25.0\ \mathrm{au},$$

$$T(r) = 18.7\ [\mathrm{K}]\left(\frac{r}{400\ [\mathrm{au}]}\right)^{-0.14}. \qquad (13)$$

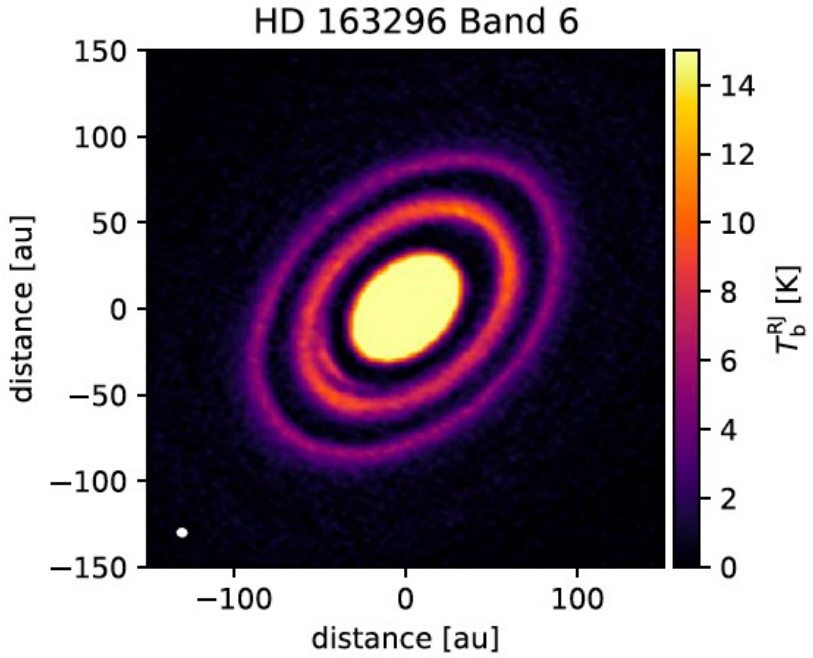

Figure 4. Image of dust continuum of HD 163296 with ALMA Band 6 (λ = 1.25 mm). We use the brightness temperature, assuming the Rayleigh–Jeans law as a representation of intensity to preserve its linearity with the observed intensity.

HD163296 モデル

半径方向

$$\Sigma_{dust}(r) = \Sigma_{disk}\exp[-(r/r_{disk})^5] + \Sigma_{ring1}\exp[-(r - r_{0,ring1})^2/2w_{ring1}^2] + \Sigma_{ring2}\exp[-(r - r_{0,ring2})^2/2w_{ring2}^2]. \qquad (14)$$

厚み方向
- ガスの厚み方向は静水圧平衡($h_{gas} = c_k/\Omega_{kep}$)
- ダストの厚みはパラメーター f_{set}でfittingして調べる($f_{set} = h_{gas}/h_{dust}$)

輻射輸送計算結果

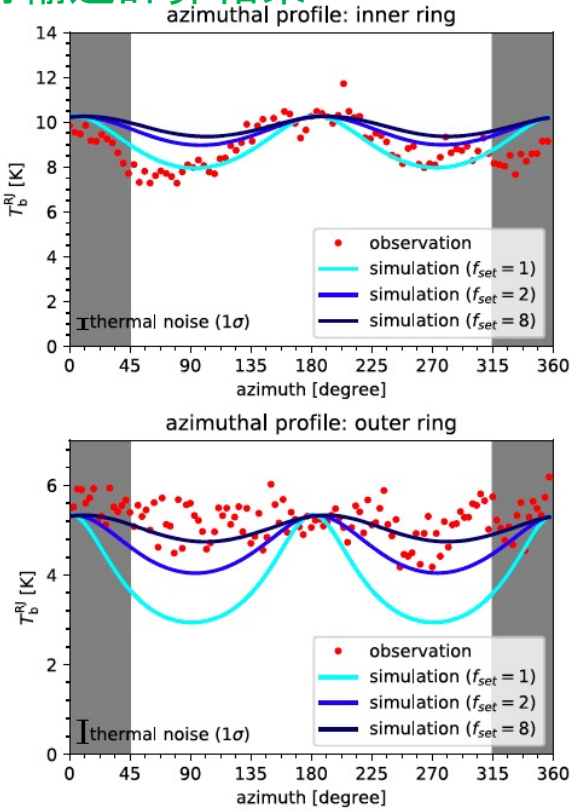

Figure 6. Azimuthal intensity variation along the ridge. The red dots show the observations, and the solid lines represent the simulations. The black, blue, and cyan line indicate $f_{set} = 1$ (no settling), 2 and 8, respectively. The shaded regions represent the areas with non-axisymmetric features such as a crescent. We plot the data at every FWHM of the beam (Huang et al. 2018).

議論

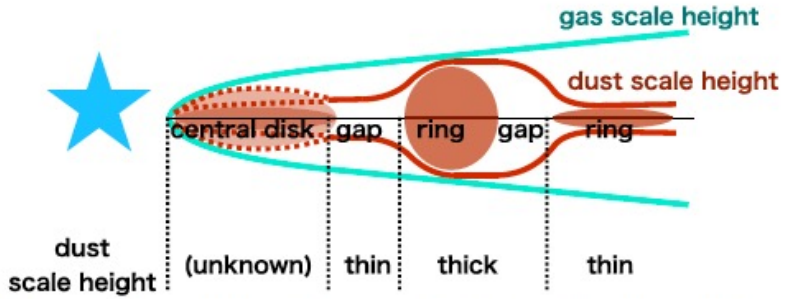

Figure 11. Schematic view of the dust scale height for the entire region. The scale height in the gaps is taken from Ohashi & Kataoka (2019), and the scale height in the rings is from our study. The dust scale height of the central disk remains unknown.

乱流とStでの考察

垂直方向の沈殿と乱流拡散がバランスしてると仮定(St≪1なら)、

$$h_d = \left(1 + \frac{\mathrm{St}}{\alpha}\right)^{-1/2} h_g, \qquad (16)$$

内リングで $\alpha/\mathrm{St} > 2.4$
外リングで $\alpha/\mathrm{St} < 1.1 \times 10^{-2}$

外リングでは(内リングに比べ)乱流が強いorダストが少ない?

fitting

$f_{\mathrm{set}} = h_{\mathrm{gas}}/h_{\mathrm{dust}} \sim 1.1$ for inner ring
$f_{\mathrm{set}} = h_{\mathrm{gas}}/h_{\mathrm{dust}} > 9.5$ for outer ring
内リングのダストはフレア、外リングのダストは沈殿？

Two-component Magnetic Field along the Line of Sight to the Perseus Molecular Cloud: Contribution of the Foreground Taurus Molecular Cloud

Y. Doi, T. Hasegawa, P. Bastien, M. Tahani, D. Arzoumanian, S. Coudé, M. Matsumura, S. Sadavoy, C. L. H. Hull, Y. Shimajiri, R. S. Furuya, D. Johnstone, R. Plume, S. Inutsuka, J. Kwon, M. Tamura

https://arxiv.org/pdf/2104.11932.pdf

若い星形成領域Perseus分子雲のPlanck偏波観測データとGaia距離測定データを用いることで、B-field方向が300pcと150pcという異なる距離のbi-modal分布であることを示す。手前の分子雲は薄くTaurus座分子雲の外縁にある。また、Perseus分子雲とTaurus分子雲の間にPer OB2 associationに付随する100-160pcサイズのダストキャビティーも同定した。

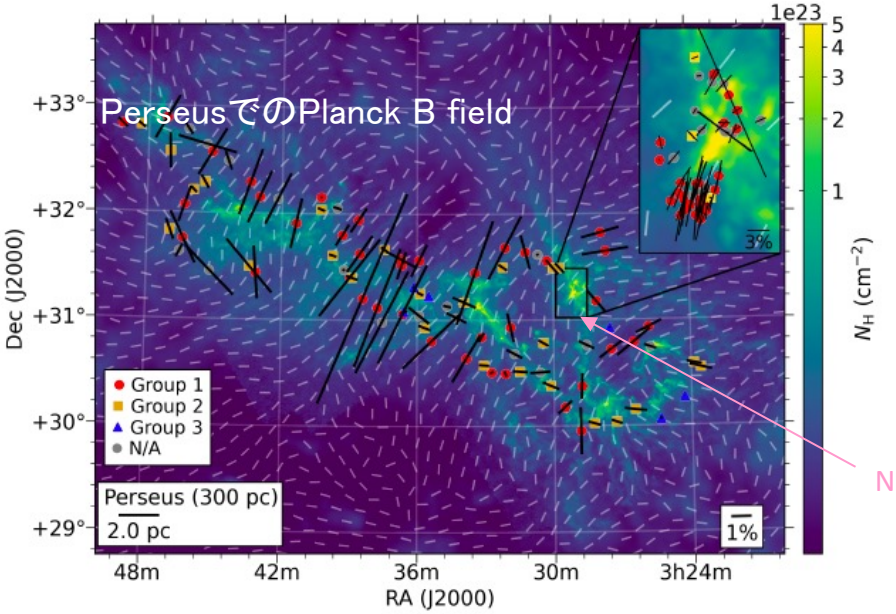

Figure 1. Perseus Planck B-Field
黒線は、星減光による偏波方向(B fieldでは?)

Table 1. θ_{star} and P_{star} Values of Each Distance Group obtained from Optical Polarimetry Data (Goodman et al. 1990)

	Distance (pc)	N_{star}[a]	θ_{star}[b] (deg)	P_{star} (%)
Group 1	> 300	39	−37.6 ± 35.2	2.0 ± 1.7
Group 2	150 – 300	25	+66.8 ± 19.1	0.8 ± 0.6
Group 3	< 150	6	−41.8 ± 32.0	0.1 ± 0.1

Gaiaなどによる距離測定でのGroup分け(111 sources)

Group分けと偏波のposition angle

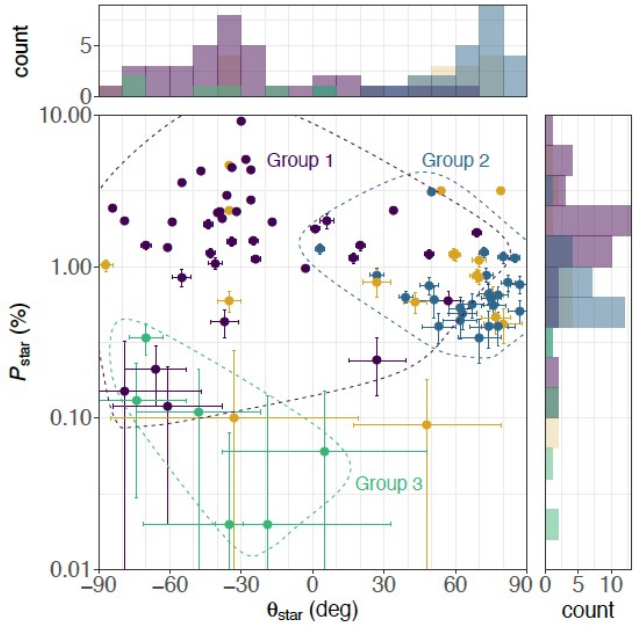

Figure 2. A correlation between θ_{star} and P_{star} of the optical polarimetry by Goodman et al. (1990). Histgrams of the two parameters are also shown on each axis. Color codes are the stellar distance ranges same as Figure 1. Yellow data points are the data with no reliable distance estimation available.

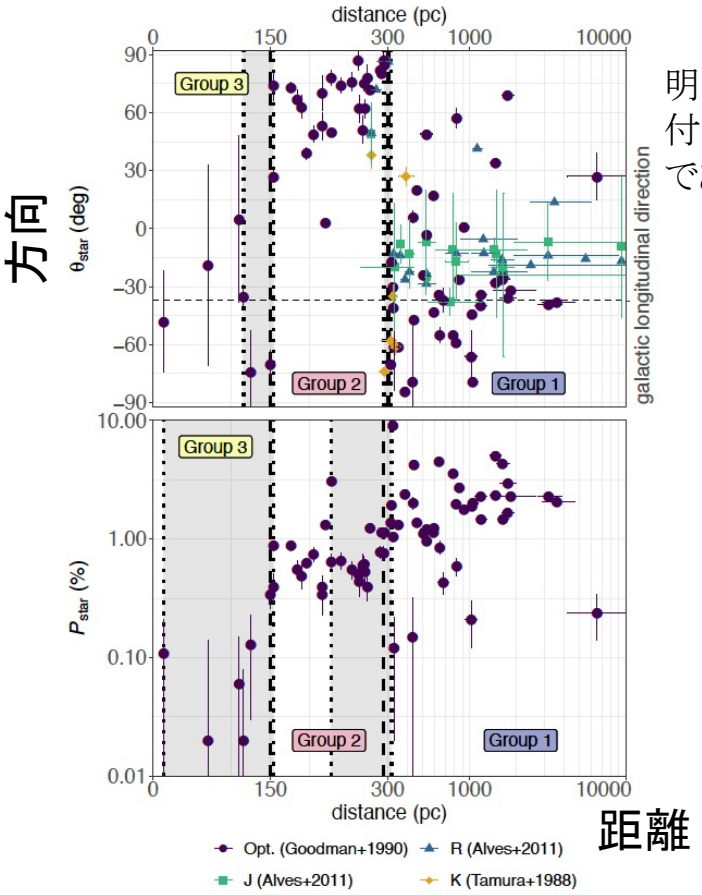

方向

距離

明らかに距離~300pc付近でbi-modal分布である。